Mechanical Systems and Signal Processing 135 (2020) 106428

Contents lists available at ScienceDirect

Mechanical Systems and Signal Processing

journal homepage: www.elsevier.com/locate/ymssp

Nonlinear sound absorption of ultralight hybrid-cored sandwich panels

Yufan Tang [a,b], Wei He [a,b], Fengxian Xin [a,*], Tian Jian Lu [b,c,*]

[a] State Key Laboratory for Strength and Vibration of Mechanical Structures, Xi'an Jiaotong University, Xi'an 710049, PR China
[b] State Key Laboratory of Mechanics and Control of Mechanical Structures, Nanjing University of Aeronautics and Astronautics, Nanjing 210016, PR China
[c] Nanjing Center for Multifunctional Lightweight Materials and Structures (MLMS), Nanjing University of Aeronautics and Astronautics, Nanjing 210016, PR China

ARTICLE INFO

Article history:
Received 22 April 2019
Received in revised form 18 September 2019
Accepted 5 October 2019
Available online 16 October 2019

Keywords:
Nonlinear sound absorption
Ultralight structure
Hybrid-cored
Sandwich panel

ABSTRACT

A combined experimental, numerical and analytical approach is employed to investigate the nonlinear effect of incident sound pressure level (SPL) on the sound absorption performance of a novel ultralight sandwich panel with perforated honeycomb-corrugation hybrid (PHCH) core. Built upon the motion, continuity and heat conduction equations for compressible viscous fluids, the numerical model fully considers the nonlinear effects caused by incident sound wave with high SPL. The analytical model is constructed by using an approximation solution to the characteristic impedance of micro-perforated panel (MPP) absorbers with consideration of the compressibility of the fluid inside the perforation. The validity of both the numerical and analytical models is checked against experimental measurement results. The effects of facesheet thickness, corrugation thickness and core height on sound absorption are systematically explored. The proposed PHCH sandwich construction is ultralight. It has small total thickness and possess simultaneous load-bearing, energy absorption and sound absorption properties, showing great potential in multi-functional applications. This work provides a nonlinear analytical model and a nonlinear numerical method for the sound absorption of the ultralight hybrid-cored sandwich structures, which demonstrates their superior performance against sound with high SPL.

© 2019 Elsevier Ltd. All rights reserved.

1. Introduction

Sandwich structures are typically known for their high specific stiffness/strength. In recent years, a variety of novel sandwich structures having multifunctional attributes have been developed for applications such as electromagnetic shielding [1,2], thermal insulation [3,4] and sound attenuation [5,6]. For instance, while honeycomb sandwich constructions have been successfully exploited for long as lightweight load-bearing structures [7,8], their sound transmission loss behaviors also received considerable interest [9,10]. Zhou and Croker [9] made comparisons between experimental and analytical results of sound transmission loss for foam-filled honeycomb sandwich panels, finding that the radiation loss of clamped sandwich panels is large near the critical frequency, especially for thin sandwich panels. The honeycomb sandwich can also become an efficient sound absorber if one of its facesheets is perforated with sub-millimeter holes, and these micro-perforations do not deteriorate appreciably the great mechanical properties of the sandwich. This type of sandwich has also been termed as the micro-perforated panel (MPP) absorber backed by honeycomb [11–13].

* Corresponding authors.
E-mail addresses: fengxian.xin@gmail.com, fxxin@mail.xjtu.edu.cn (F. Xin), tjlu@nuaa.edu.cn (T.J. Lu).

https://doi.org/10.1016/j.ymssp.2019.106428
0888-3270/© 2019 Elsevier Ltd. All rights reserved.

Most existing studies on the acoustic properties of sandwich structures are based on the fluid incompressibility hypothesis. When the sound pressure level (SPL) of an incident sound wave is sufficiently high, the fluid can no longer be regarded as incompressible. For example, the SPL over an acoustic lining for turbofan duct can be as high as 150 dB [14]. The performance of a sound absorber at high SPLs differs greatly from that at low SPLs. The nonlinear acoustic impedance of MPPs has been studied by Maa [15]. He used the motion equation for compressible viscous fluid to describe the velocity and pressure fields within the perforations, and obtained the relationship between the impedance and the maximum of particle vibration velocity. Park [16] investigated the performance of MPPs in a high sound pressure environment using an empirical acoustic resistance model, finding that a poor sound absorption at low SPLs can be a good one at high SPLs. Xu and coauthors [17] also proposed a modified nonlinear impedance model to capture the main characteristics of the resonator. At present, only a few researches are focused on sound absorption under high SPLs, and there is pressing need for analytical and numerical models of acoustic sandwich structures.

As aforementioned, researchers have investigated the nonlinear effects for MPP absorbers, but no existing studies consider the nonlinear sound absorption of hybrid-cored sandwich panels. Up to now, it still lacks accurate analytical and numerical models for nonlinear effects of complex sandwich structures against sound with high SPL. The focus of the present study is placed upon quantifying the nonlinear sound absorption behavior of the MPP-type sandwich panels using a combined analytical, numerical and experimental approach. Specifically, the sandwich panel has a honeycomb-corrugation hybrid core, which has previously been demonstrated to possess both great specific compressive strength and extraordinary energy absorption capability [18]. By further perforating its facesheet and corrugation, this type of sandwich construction also exhibits huge sound absorption potentials [19,20]. In the current study, to further investigate the sound absorption performance of the perforated honeycomb-corrugation hybrid (PHCH) core under high SPLs, the compressibility of fluid is accounted for both analytically and numerically. To validate the analytical and numerical results, standard experimental measurements are carried out.

2. Nonlinear numerical model

Fig. 1(a) illustrates the ultralight sandwich panel with PHCH core, which is composed of a periodically perforated top facesheet, a non-perforated bottom facesheet, and prismatic honeycomb blocks inserted into a corrugated core, the latter also periodically perforated. Fig. 1(b) displays the half section view of its unit cell which, in total, contains six honeycomb blocks. For generality, the six circular perforations on the top facesheet are assumed to have different diameters, denoted here as diameters $d_{n,1}$ ($n = 1, 2, \ldots, 6$). Similarly, four different perforation diameters $d_{n,2}$ ($n = 2, 3, 5, 6$) on the corrugation are assumed. Let the inner length of a honeycomb block be denoted by b_1 and the cell length by b_2. Let the facesheet thickness be denoted by t_f and the corrugation thickness by t_c. The height of the hybrid core is taken as D.

The numerical model of the PHCH unit cell is established essentially on the basis of the linear Navier-Stokes (N-S) physics model in COMSOL Multiphysics. However, as the N-S equations in the original model are for incompressible viscous fluids only, these equations need to be modified to account for nonlinear effects, as [21]:

$$\begin{aligned} & j\omega\rho + \mathbf{u}\nabla\cdot\rho + \rho\nabla\cdot\mathbf{u} = 0 \\ & \rho_0(j\omega\mathbf{u} + \mathbf{u}\nabla\mathbf{u}) - \nabla\cdot\left\{-p\mathbf{I} + \eta\left[\nabla\mathbf{u} + (\nabla\mathbf{u})^{\mathrm{T}} - \left(\tfrac{2}{3}\eta - \eta_B\right)(\nabla\cdot\mathbf{u})\mathbf{I}\right]\right\} = 0 \\ & \rho_0 C_p(j\omega T + \mathbf{u}\nabla T) - \alpha_0 T_0(j\omega p + \mathbf{u}\nabla p) - \nabla\cdot(\kappa\nabla T) = 0 \end{aligned} \tag{1}$$

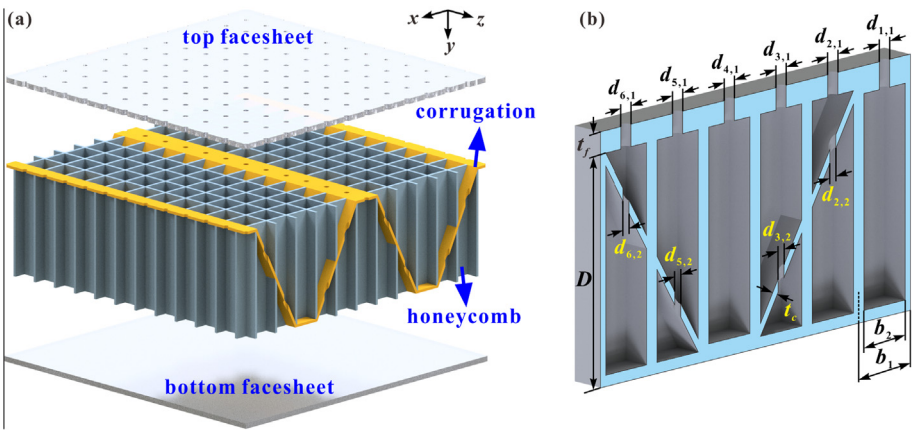

Fig. 1. (a) Schematic of PHCH sandwich panel; (b) half section view of a unit cell in PHCH.

where ρ, T and p refer to the variations of air density, temperature and air pressure; $\mathbf{u}$ and $\mathbf{I}$ are the vibration velocity of the particle and the identity matrix, and $()^{\mathrm{T}}$ denote the transposition of a matrix; η_B, C_p, α_0 and κ are separately the bulk viscosity, specific heat at constant pressure, thermal expansion coefficient and thermal conductivity of air; ρ_0 and T_0 refer to the density of air and the surrounding temperature; η is the dynamic viscosity of air; and j and ω are the imaginary unit and the angular frequency of incident sound wave, respectively. In the current study, ρ_0 = 1.213 kg·m^{-3}, T_0 = 293.15 K and η = 1.871 × 10^{-5} Pa·s.

The relationship among the density, temperature and pressure of the air can be written as:

$$\rho = \rho_0(\beta_T p - \alpha_0 T) \tag{2}$$

where β_T is the isothermal compressibility of air, while α_0 and β_T satisfy:

$$\begin{aligned} \beta_T &= \frac{\gamma}{\rho_0 \cdot c_0^2} \\ \alpha_0 &= c_0 \cdot \sqrt{\frac{C_p \cdot (\gamma - 1)}{T}} \end{aligned} \tag{3}$$

in which γ is the specific heat ratio of air.

No slip and isothermal boundary conditions are applied on the surface of the considered structure (Fig. 1). The incident sound wave is simulated using the pressure (adiabatic) condition. Upon calculating the pressure and velocity fields in the structure using the above numerical model, the surface impedance ratio is calculated as:

$$z_s = \frac{\langle p \rangle_s}{\langle v_y \rangle_s} \cdot \frac{1}{Z_0} \tag{4}$$

where $\langle p \rangle_s$ and $\langle v_y \rangle_s$ refer to the averaged sound pressure and averaged particle velocity along the y direction (i.e., axial direction of the perforation, see Fig. 1) on the surface of the structure. And Z_0 refers to the characteristic impedance of the air.

Once the surface impedance ratio is obtained, the sound absorption coefficient of the PHCH sandwich panel is determined as:

$$\alpha = 1 - \left| \frac{z_s - 1}{z_s + 1} \right|^2 \tag{5}$$

Perfect sound absorption occurs only when the real part of the surface impedance ratio equals to 1 and the imaginary part equals to 0.

Fig. 2 presents the finite element (FE) model for COMSOL Multiphysics. The upper portion of the FE model represents the incident field, which is employed to generate the incident acoustic pressure. The lower portion refers to the fluid both in the perforations and cavity of the PHCH. For numerical accuracy, the FE mesh is sufficiently refined in the perforation areas both on the facesheet and the corrugation. The cavity parts of the FE model are meshed with tetrahedral elements, while the perforation parts are meshed by swept meshing of triangular elements.

As previously mentioned, at the boundary of the FE model in Fig. 2, no slip and isothermal condition are applied, as:

$$\begin{aligned} \mathbf{u} &= 0 \\ T &= 0 \end{aligned} \tag{6}$$

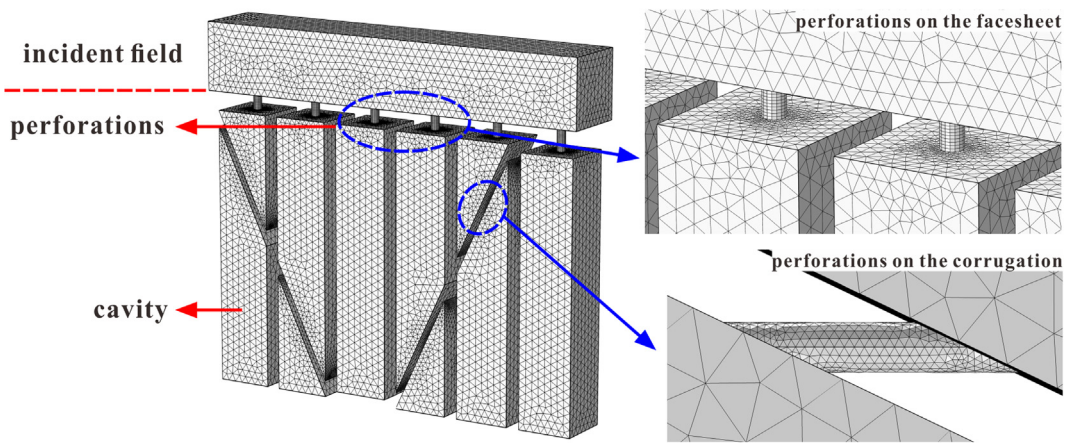

Fig. 2. Finite element model of a unit cell in PHCH.

3. Nonlinear analytical model

In addition to the numerical model as detailed in the previous section, analytical modeling based upon the Maa's model for micro-perforated panel (MPP) absorbers is also established for the proposed structure of Fig. 1. The original Maa model, also based on the N-S equations, was constructed by solving the velocity field inside a small cylindrical tube:

$$\rho_0\dot{u} - \frac{\eta}{r}\frac{\partial}{\partial r}\left(r\frac{\partial}{\partial r}u\right) = \frac{\Delta p}{l} \tag{7}$$

in which Δp, l, u, and r denote the sound pressure difference between the two ends of the tube, the length of the tube, the axial particle velocity of the air in the tube, and the radius vector, respectively.

By combining the solution given by Crandall [22] and the end correction given by Kosten and Zwikker [23], Maa proposed a simple form of equations to calculate the acoustic impedance of a typical MPP [24]. With reference to Fig. 1(b), based on the Maa model, the acoustic impedance of the n-th perforation on the m-th layer may be obtained, as:

$$Z_{Mn,l} = \frac{32\eta t_l}{d_{n,l}^2}\left(1 + \frac{\omega\rho_0 d_{n,l}^2}{128\eta}\right)^{0.5} + j\omega\rho_0 t_l\left[1 + \left(9 + \frac{\omega\rho_0 d_{n,l}^2}{8\eta}\right)^{-0.5}\right] + \frac{\sqrt{2\omega\rho_0\eta}}{2} + E_c \tag{8}$$

where $E_c = \sqrt{2\omega\rho_0\eta}/2 + 0.85j\omega\rho_0 d$ is the end correction. Here, for the panel thickness of the m-th layer t_l (l = 1, 2), t_1 equals to t_f and t_2 equals to t_c. The surface impedance of the n-th honeycomb block on the l-th layer $Z_{n,l}$ may thence be calculated, as:

$$Z_{n,l} = \frac{Z_{Mn,l}}{\varphi} + Z_{Cn,l} \tag{9}$$

where φ, $Z_0 = \rho_0 c_0$ and D refer separately to the porosity of the MPP, the characteristic impedance of the air and the depth of the cavity behind the MPP. $Z_{Cn,l}$ is the acoustic impedance of the n-th cavity in the l-th layer, which satisfies:

$$\begin{cases} Z_{Cn,1} = Z_0\frac{Z_{n,2}\cos(kD_{n,1}) + jZ_0\sin(kD_{n,1})}{Z_0\cos(kD_{n,1}) + jZ_{n,2}\sin(kD_{n,1})}, & n = 2,3,5,6 \\ Z_{Cn,1} = -jZ_0\cot(kD_{n,1}), & n = 1,4 \\ Z_{Cn,2} = -jZ_0\cot(kD_{n,2}), & n = 2,3,5,6 \end{cases} \tag{10}$$

In the equations above, the subscript C means cavity and $k = \omega/c_0$ is the wave number of the incident sound wave.

The total surface impedance of the PHCH sandwich is derived as follows:

$$Z_s = 6\delta_H \cdot \left(\sum_{n=1}^{6}\frac{1}{Z_{n,1}}\right)^{-1} \tag{11}$$

where $\delta_H = b_1^2/b_2^2$ is correction factor relating to the thickness of the honeycomb wall, which is introduced to account for the influence of honeycomb cell-wall thickness on the surface impedance of the whole structure. Once the total surface impedance is determined using Eqs. (7)–(10), the sound absorption coefficient of the PHCH sandwich under low SPL conditions is determined.

To fully evaluate the nonlinear effects caused by the incident acoustic wave with high SPL, the motion equation for a compressible viscous fluid is needed to consider fluid compressibility, as:

$$\rho\dot{u} + \rho u\frac{\partial u}{\partial x} - \frac{\eta}{r}\frac{\partial}{\partial r}\left(r\frac{\partial}{\partial r}u\right) = \frac{\Delta p}{t} \tag{12}$$

Apart from the motion equation, the continuity equation is also needed, as:

$$\dot{\rho}t + u\frac{\partial\rho}{\partial x} + \rho\frac{\partial u}{\partial x} = 0 \tag{13}$$

From Eqs. and , the acoustic impedance of a typical MPP can be acquired. However, no analytic solution can be obtained. Maa proposed an approximate method to evaluate the surface impedance of the MPP absorber under high SPL [15], as:

$$z_{s-spl} = z_s + \frac{u_0}{\varphi c_0} + \frac{0.85j\omega d}{\varphi c_0}\left(\frac{1}{1 + u_0/\varphi c_0} - 1\right) \tag{14}$$

in which $z_s = Z_s/Z_0$ is the specific surface impedance and u_0 satisfies:

$$p_{in} = \frac{\varphi p_0}{2}\cdot\frac{u_0}{c_0}\left(1 + Re(z_s) + \frac{u_0}{\varphi c_0}\right) \tag{15}$$

In the equations above, c_0=343 m·s^{-1} and p_0 = 101325 Pa represent the sound speed in the air and the ambient pressure, and p_{in} refers to the incident acoustic pressure which can be expressed as:

$$p_{in} = 10^{\frac{dB}{20}} \cdot p_{ref} \tag{16}$$

Equation relates the sound pressure to the SPL: dB signifies the SPL and p_{ref} is the reference sound pressure. Commonly used reference sound pressure is 2×10^{-5} Pa in air and 1×10^{-6} Pa in water.

4. Fabrication and experiment

The fabrication processes of a PHCH sample are illustrated in Fig. 3. The thickness of the honeycomb plates in Fig. 3(a) and the width of the periodically arranged slits in each plate in Fig. 3(b) are both taken as t_w. The distance between two adjacent slits is b_1, which decides the size of the trapezoidal honeycomb block to be cut from the brazed honeycomb of Fig. 3(c) and then inserted into the corrugation (i.e., the folded plate) of Fig. 3(e). The inner length of the honeycomb block b_2 is equal to $b_1 - t_w$. The trapezoidal honeycomb cores are designed to just fit the folded plate, the thickness of which being t_c. By brazing them and a facesheet (thickness t_f) together, a panel with honeycomb-corrugation hybrid core is made, as shown in Fig. 3(f). Let the height of the hybrid core be D, which is the same as the width of the honeycomb plate as well as the height of the corrugation. The thickness of the whole panel is then $D + t_f$. The last step of fabrication is perforating, as shown in Fig. 3(g). By drilling both the facesheet and the corrugation by a laser, a PHCH sample can finally be fabricated. It must be mentioned here that, as the sample is to be placed inside a B&K PULSE Acoustic Material Testing System, without any cavity allowed between it and the end plate of the Testing System, a second facesheet is not added to the sample.

In the current study, the geometrical parameters of the fabricated sample for acoustic testing are the same as those of Sample A listed in Table 1. For simplicity, the perforations on the facesheet as well as on the corrugation have identical parameters, 0.5 mm. The other sample, Sample B in Table 1, is not fabricated and only used in subsequent numerical and analytical calculations for the purpose of comparison. Actually, the configurations of Sample A and Sample B are the same, but with different dimensional parameters.

The sound absorption experiments are performed using the B&K PULSE Acoustic Material Testing System. The experimental facility and diagrammatic sketch are illustrated in Fig. 4. The measuring processes are integrated in the system, which follows the standard of ISO 10534–2 [25]. Fig. 5 displays Sample A and its macroscopic sizes. The test sample has a diameter of 100 mm, which is used to measure acoustic properties from 50 Hz to 1600 Hz.

Fig. 6 compares the experimental, analytical and numerical results for the sound absorption coefficient of Sample A. The experimental results are presented from 200 Hz to 1600 Hz, since the results below 200 Hz are severely fluctuating due to

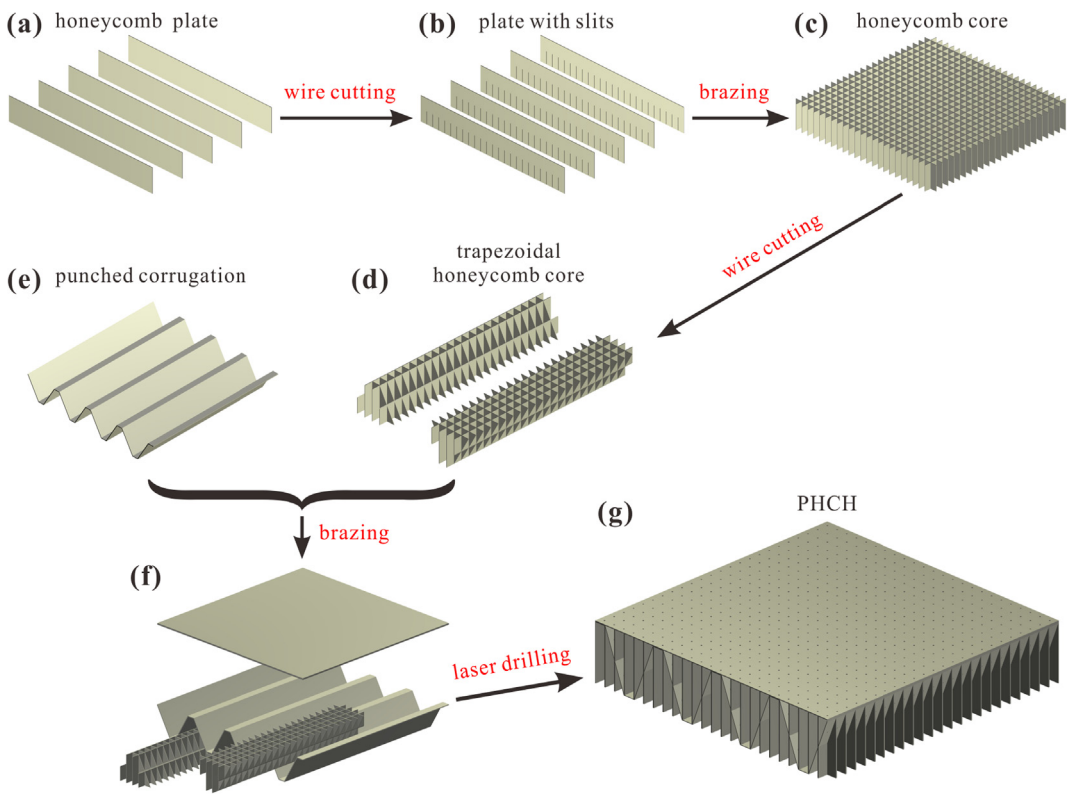

Fig. 3. Fabrication processes of a PHCH sample.

Table 1
Geometrical parameters of samples.

	Sample A	Sample B
d_{11}/mm	0.5	0.4
d_{21}/mm	0.5	0.4
d_{31}/mm	0.5	0.5
d_{41}/mm	0.5	0.5
d_{51}/mm	0.5	0.6
d_{61}/mm	0.5	0.6
d_{22}/mm	1.0	0.2
d_{32}/mm	1.0	0.2
d_{52}/mm	1.0	0.3
d_{62}/mm	1.0	0.3
t_f/mm	0.5	0.5
t_c/mm	0.5	0.2
b_1/mm	5.0	4
b_2/mm	4.8	3.8
D/mm	18	24

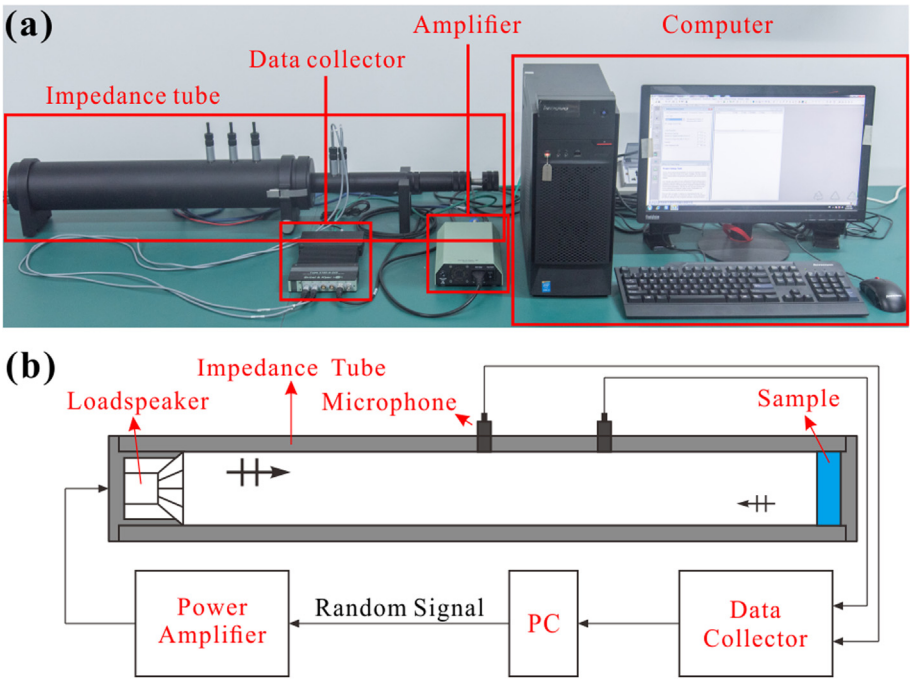

Fig. 4. Experimental setup for measuring sound absorption with B&K PULSE Acoustic Material Testing System: (a) Experimental facility; (b) Diagrammatic sketch.

instrumental errors. In Fig. 6, Signal A and Signal B refer to the signals of the sound pressure levels tested by the two microphones in the B&K standing wave tube. The error bars are based on the experimental results to assess the differences from both the analytical and numerical results. Generally speaking, the results are acceptable in low-and-intermediate frequency range. In particular, a good prediction of the theory and a good agreement of all the three results are reached at the peak frequency and the peak value. However, the differences become larger after the peak frequency.

The difference between analytical results and experimental results is further analyzed. The experimental results of the imaginary part for the surface acoustic impedance ratio are lower than the analytical ones in the whole frequency band, as shown in Fig. 7(a). By contrast, there is almost no difference between the two real parts when the frequency is higher than 600 Hz. Consequently, it is believed that the dissimilarities in sound absorption coefficients originate from the difference in the imaginary part, as demonstrated in Fig. 7(b).

When the sample is fabricated during the procedure of brazing, the solder will more or less occupy the cavity of the PHCH, reducing thus the cavity space relative to the design target. Correspondingly, the equivalent cavity depth D is also reduced. From the analytical equations listed in the previous section, it can be seen that the imaginary part of the surface impedance decreases with decreasing cavity depth. Therefore, the source for the differences in Fig. 6 is mainly attributed to the smaller cavity depth induced by brazing during fabrication.

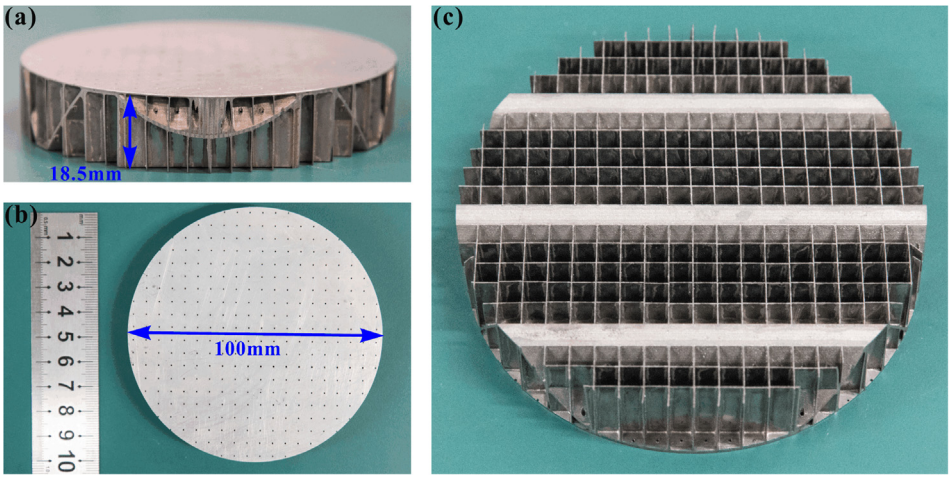

Fig. 5. Test sample of PHCH (Table 1): (a) front view; (b) top view; (c) bottom view.

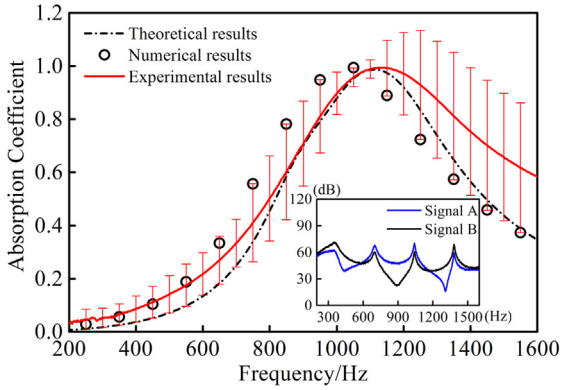

Fig. 6. Experimental, analytical and numerical results for sound absorption coefficient of sample A.

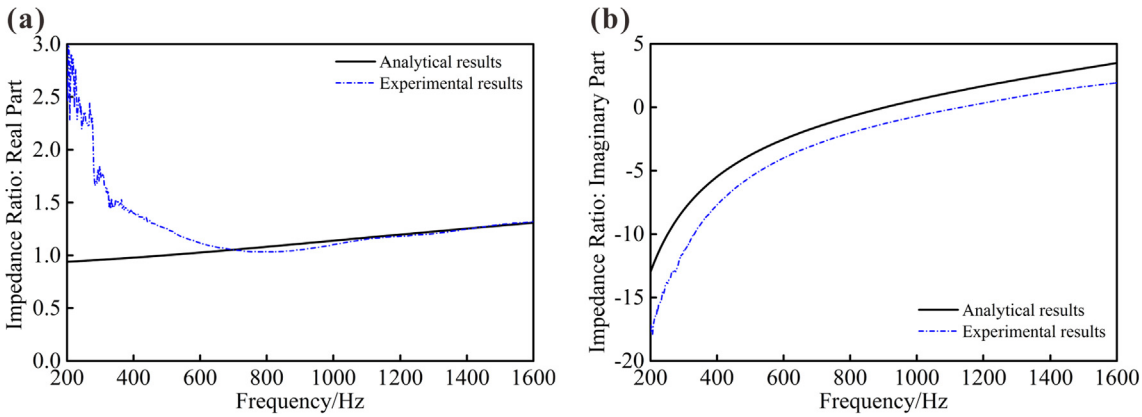

Fig. 7. Comparison between analytical predicted and experimentally measured surface impedance ratio: (a) real part; (b) imaginary part.

5. Results and discussion

In order to study the relationship between the distribution of fluid field in the PHCH structure and the SPL of the incident sound wave, Fig. 8 displays the numerically simulated velocity distribution of fluid particles at 1250 Hz under different SPLs. As the SPL gradually intensifies, the vibration velocity of particles both in the perforation areas and the cavity areas becomes

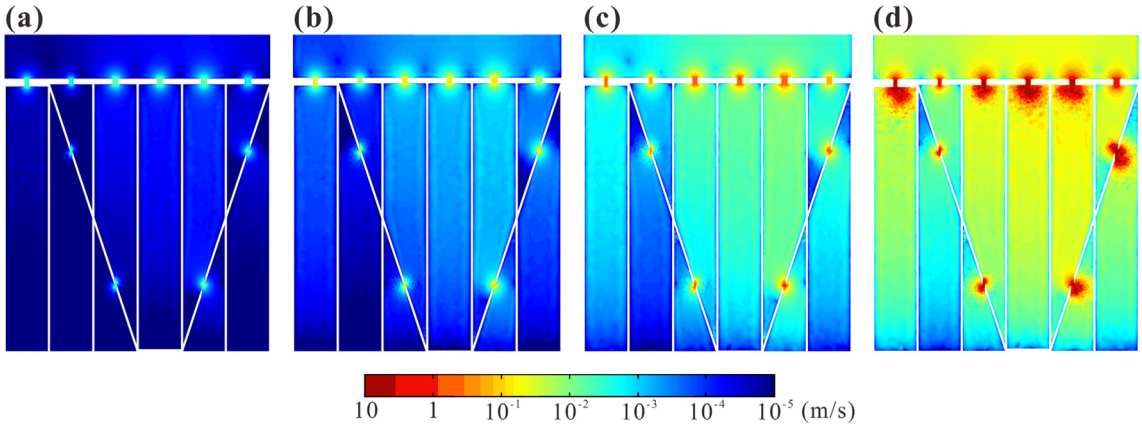

Fig. 8. Numerically simulated nephogram for vibration velocity of particles inside PHCH for selected SPL levels: (a) 60 dB; (b) 80 dB; (c) 100 dB; (d) 120 dB.

greater. According to the present specific data, every 20 dB contributes to about one order of magnitude in the increase of vibration velocity.

Besides, it is seen that the vibration velocity is maximized in narrow areas so that the color surrounding the perforation regions is the reddest, implying that the velocity in the perforations is at least two orders of magnitude larger than that in the cavity. As a matter of fact, in the current PHCH construction, one perforation and the honeycomb cavity below it constitute a classical Helmholtz resonator. When the frequency of sound approaches the resonant frequency of this resonator, fluid particles in narrow areas will vibrate greatly. With severe vibration of fluid particles in the perforation areas, the acoustic energy is more efficiently transformed into thermal energy via viscous boundary layer. This process is the main physical mechanism underlying the sound absorption performance of PHCH-like structures.

Upon performing statistical analysis on the numerical results, the averaged vibration velocity in the perforations is obtained and plotted in Fig. 9 as a function of SPL. The averaged vibration velocity increases, nonlinearly, as the SPL is gradually increased. Special attention is needed at the turning point, which is approximately 90 dB in this study. Before 90 dB, the average velocity is approximately equal to 0. However, once the SPL exceeds 90 dB, the vibration velocity begins to increase drastically. The velocity at 120 dB is several orders of magnitude greater than that at 60 dB and 90 dB.

Next, by using the parameters of Sample B (Table 1), the analytically predicted and numerically calculated sound absorption coefficients at 60 dB and 120 dB are displayed in Fig. 10. Good agreement between the analytical predictions and numerical results is achieved. Although the SPL has almost no influence on sound absorption under 60 dB, the present results obtained for the case of 60 dB still consider the compressibility of air. Fig. 10 also presents the analytical results at 90 dB, which are quite close to the results at 60 dB. This again validates that 90 dB is critical: when the SPL is lower than 90 dB, its variation has little influence on sound absorption.

The results of Fig. 10 demonstrate that the magnitude of SPL has great influence on the sound absorption performance of the proposed PHCH sandwich structure: the sound absorption versus frequency curve is smoother and the half sound absorption bandwidth becomes wider at a higher SPL (>90 dB). However, the peak value of sound absorption decreases as the SPL is increased, thus unable to reach perfect absorption. Simultaneously, the frequency at which the absorption reaches the peak increases with increasing SPL.

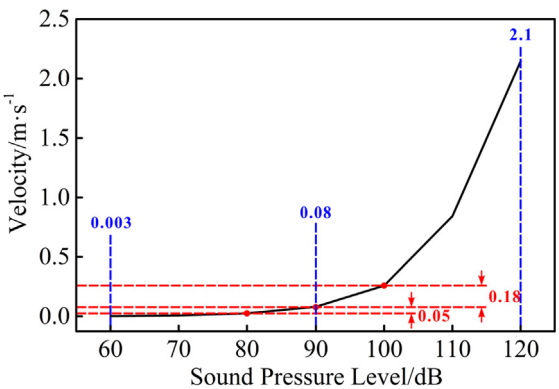

Fig. 9. Averaged vibration velocity of particles inside perforations from 60 dB to 120 dB.

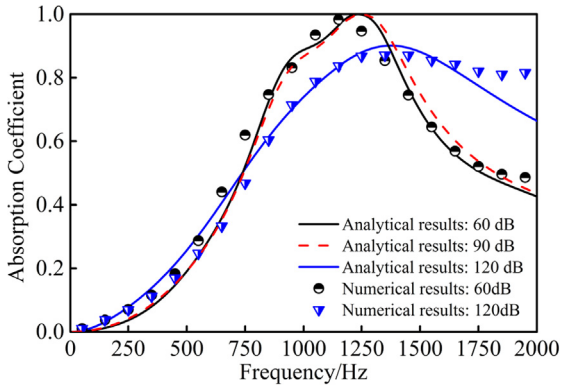

Fig. 10. Comparison of analytically predicted and numerically calculated sound absorption versus frequency curves for selected SPL levels of 60 dB, 90 dB and 120 dB.

To further explore the sound absorption characteristics of the PHCH at different SPLs, surface impedance analysis is performed with the analytical model. From Eq. (14), it can be seen that with the increasing of u_0 (associated with high SPL), the real part of the specific surface impedance increases and the imaginary part decreases. It means that higher SPL leads to higher real specific surface impedance and lower imaginary specific surface impedance, which are demonstrated by the results in Fig. 11. Corresponding results are presented in Fig. 11. Increasing the SPL causes the real part of the surface impedance ratio to move up, thus away from the perfect absorption condition ($Re(z_s) = 1$). This is the main reason for the peak absorption value at 120 dB being smaller than that at 60 dB. At the same time, the increase of SPL causes the imaginary curve to move down, so that it passes through the perfect absorption condition ($Im(z_s) = 0$) at a higher frequency. This is the main reason for the absorption peak moves to a high frequency under a higher SPL. After the imaginary curve passes through the 0 point, the difference between the 120 dB curve and the 60 dB curve becomes increasingly large, so the former is closer to the 0 point than the latter. As a result, the half sound absorption bandwidth corresponding to the 120 dB curve is wider than that of the 60 dB curve. In addition, the real curve is gentler at 120 dB, especially near the peak frequency where the imaginary part passes through the 0 point. It contributes to the relatively smoothness of the 120 dB sound absorption curve, as can be seen from Fig. 10.

To quantify the influence of facesheet thickness on sound absorption, the average absorption coefficients from 10 Hz to 2000 Hz varying systematically with both the SPL and the facesheet thickness are presented in Fig. 12. To this end, the remaining geometrical parameters of the PHCH sample are the same as Sample B in Table 1. In Fig. 12 and the figures to follow, the deeper the red color, the larger the average sound absorption coefficient. As can be seen from Fig. 12, while the SPL is relatively low, the average sound absorption coefficient decreases with thickening facesheet. In contrast, when the SPL becomes sufficiently high, the contour lines are almost vertical to the y axis in Fig. 12, meaning that the facesheet has little influence on sound absorption. In particular, a maximum region is visible when the facesheet has a thickness of about 0.5 mm. As the facesheet thickness becomes bigger (>0.5 mm), the average sound absorption coefficient drops.

The results of Fig. 12 also demonstrate that, when the SPL is lower than 90 dB, the sound absorption performance is hardly affected by any variation in the SPL. On the contrary, the average sound absorption coefficient alters greatly once

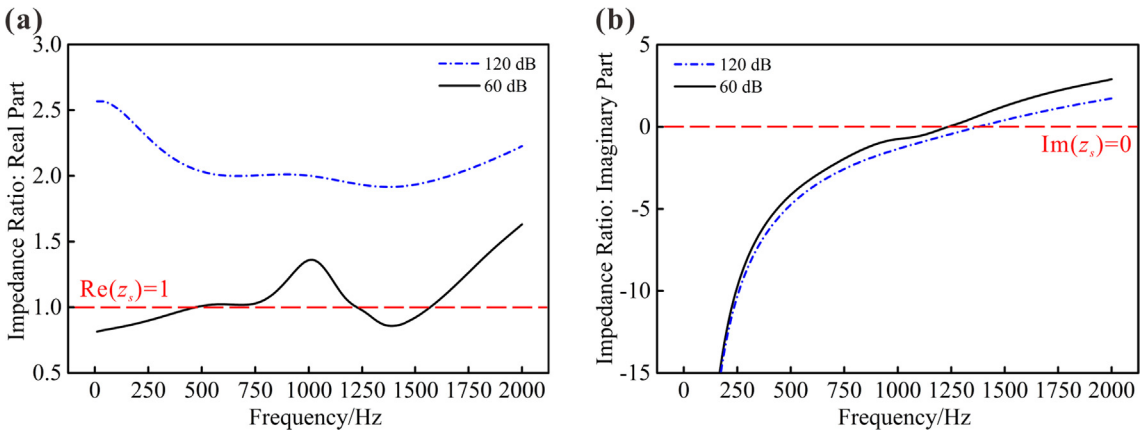

Fig. 11. Analytically predicted surface impedance ratio of PHCH at 60 dB and 120 dB: (a) real part; (b) imaginary part.

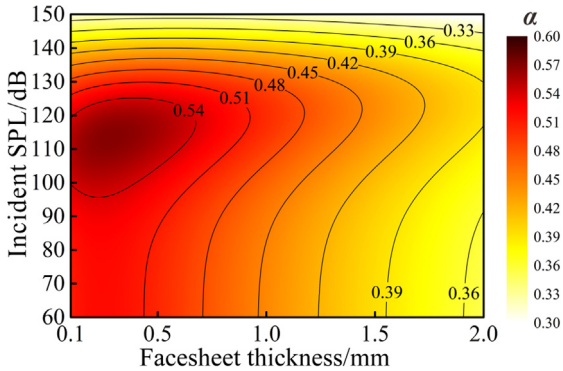

Fig. 12. Influence of facesheet thickness on averaged sound absorption coefficient from 10 Hz to 2000 Hz under different incident sound pressure levels (SPLs).

the SPL surpasses 120 dB. This phenomenon can also be demonstrated by examining how the thickness of the folded plate (the corrugation) affects the averaged sound absorption coefficient at different SPL levels. The results are presented in Fig. 13. Except for the corrugation thickness, the remaining geometrical parameters are identical as Sample B in Table 1. Similar to the facesheet thickness, it is seen from Fig. 13 that the best sound absorption requires thin corrugation with sub-millimeter thickness. However, notably different from Fig. 12, the corrugation thickness has much less influence on sound absorption when the SPL is lower than 90 dB, as there is no obvious discoloration in Fig. 13.

Besides the facesheet thickness and corrugation thickness, the core height of the PHCH structure is also found to play an important role, as displayed in Fig. 14. At any SPL from 60 dB to 150 dB, the averaged absorption coefficient is enhanced when the core becomes thicker. In the extreme when the SPL exceeds 120 dB, the averaged absorption coefficient decreases

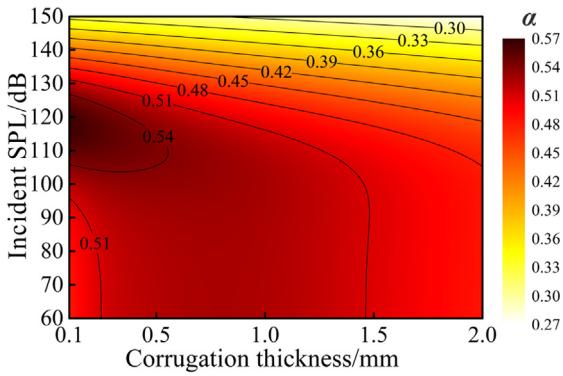

Fig. 13. Influence of corrugation thickness on averaged sound absorption coefficient from 10 Hz to 2000 Hz under different SPLs.

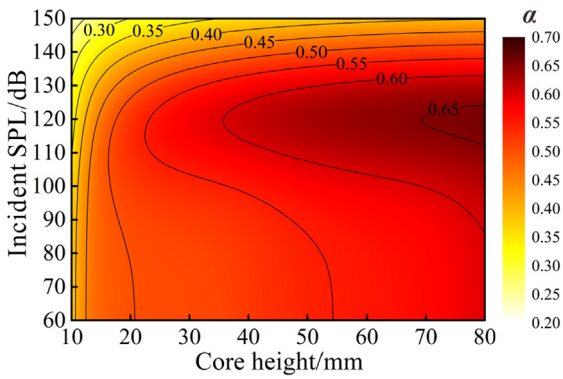

Fig. 14. Influence of core height on averaged sound absorption coefficient from 10 Hz to 2000 Hz under different SPLs.

with increasing SPL. This is attributed to the absorption peak shifting to higher frequencies as the SPL is increased, causing the major portion of the absorption curve to be located in the regime exceeding 2000 Hz.

6. Conclusion

A combined experimental, numerical and analytical approach has been used to quantify the influence of incident sound pressure level (SPL) upon the sound absorption performance of ultralight perforated honeycomb-corrugation hybrid (PHCH) core sandwich panels. To consider the nonlinear effects introduced by high SPLs, numerical simulations are performed based on differential equations for compressible viscous fluid, including the motion equation, the continuity equation and the heat conduction equation. The nonlinear analytical model is established by using an approximation theory proposed by Maa. Both the numerical simulation results and analytical model predictions agree well with the experimental measurements within the frequency range of interest. The effects of facesheet thickness, corrugation thickness and core height on the sound absorption performance of the PHCH sandwich structure are systematically explored at different SPLs. Main findings of this study are summarized as follows:

(1) As the SPL increases, the peak of the absorption curve not only becomes smaller in magnitude but also moves to higher frequencies.
(2) Brazing during the fabrication process brings a certain amount of solder into the cavity of the PHCH sample, causing the measured imaginary surface impedance smaller than the predicted one.
(3) Particles inside the perforations vibrate significantly faster when the SPL is increased beyond 90 dB.
(4) When the SPL is lower than 90 dB, the sound absorption performance is nearly independent upon the SPL. At high SPLs (>90 dB), the averaged sound absorption coefficient in the low-to-intermediate frequency range decreases sharply.

Acknowledgments

This work was supported by NSFC (11761131003, U1737107 and 11772248), DFG (ZH15/32-1) and the Fundamental Research Funds for the Central Universities (Z201811253).

References

[1] M. Hu, J. Gao, Y. Dong, et al, Flexible transparent PES/silver nanowires/PET sandwich-structured film for high-efficiency electromagnetic interference shielding, Langmuir 28 (18) (2012) 7101–7106.
[2] W.L. Song, M.S. Cao, M.M. Lu, et al, Flexible graphene/polymer composite films in sandwich structures for effective electromagnetic interference shielding, Carbon 66 (1) (2014) 67–76.
[3] T. Kawasaki, S. Kawai, Thermal insulation properties of wood-based sandwich panel for use as structural insulated walls and floors, J. Wood Sci. 52 (1) (2006) 75–83.
[4] B.J. Lee, S. Pessiki, Thermal performance evaluation of precast concrete three-wythe sandwich wall panels, Energy Build. 38 (8) (2006) 1006–1014.
[5] H. Meng, M.A. Galland, M. Ichchou, et al, Small perforations in corrugated sandwich panel significantly enhance low frequency sound absorption and transmission loss, Compos. Struct. 182 (2018) 1–11.
[6] F.X. Xin, T.J. Lu, Sound radiation of orthogonally rib-stiffened sandwich structures with cavity absorption, Compos. Sci. Technol. 70 (15) (2010) 2198–2206.
[7] H.N.G. Wadley, Multifunctional periodic cellular metals, Philos. Trans. R. Soc. A 364 (1838) (2006) 31–68.
[8] S.P. Mai, N.A. Fleck, T.J. Lu, Optimal design of box-section sandwich beams in three-point bending, Int. J. Solids Struct. 44 (14–15) (2007) 4742–4769.
[9] R. Zhou, M.J. Crocker, Sound transmission loss of foam-filled honeycomb sandwich panels using statistical energy analysis and theoretical and measured dynamic properties, J. Sound Vib. 329 (6) (2010) 673–686.
[10] F.X. Xin, T.J. Lu, Analytical modeling of fluid loaded orthogonally rib-stiffened sandwich structures: sound transmission, J. Mech. Phys. Solids 58 (9) (2010) 1374–1396.
[11] K. Sakagami, K. Nakajima, M. Morimoto, et al, Sound absorption characteristics of a honeycomb-backed microperforated panel (MPP) absorber, J. Acoust. Soc. Am. 120 (5) (2006) 3146.
[12] M. Toyoda, K. Sakagami, D. Takahashi, et al, Effect of a honeycomb on the sound absorption characteristics of panel-type absorbers, Appl. Acoust. 72 (12) (2011) 943–948.
[13] C. Yang, L. Cheng, Sound absorption of microperforated panels inside compact acoustic enclosures, J. Sound Vib. 360 (2016) 140–155.
[14] W.B. Gerald, W.P. John, S.H. Alan, Advanced Turbofan Duct Liner Concepts, Langley Research Center, 1999.
[15] D.Y. Maa, Microperforated panel at high sound intensity, Acta Acustica 21 (1) (1996) 10–14.
[16] S.H. Park, A design method of micro-perforated panel absorber at high sound pressure environment in launcher fairings, J. Sound Vib. 332 (3) (2013) 521–535.
[17] J. Xu, X. Li, Y. Guo, Nonlinear absorption characteristics and micro flow physics of resonator under high sound intensity, in: 20th AIAA/CEAS Aeroacoustics Conference. Atlanta, America, 2013.
[18] B. Han, K. Qin, B. Yu, et al, Honeycomb-corrugation hybrid as a novel sandwich core for significantly enhanced compressive performance, Mater. Des. 93 (2015) 271–282.
[19] Y. Tang, F. Li, F. Xin, et al, Heterogeneously perforated honeycomb-corrugation hybrid sandwich panel as sound absorber, Mater. Des. 134 (2017) 502–512.
[20] Y. Tang, S. Ren, H. Meng, et al, Hybrid acoustic metamaterial as super absorber for broadband low-frequency sound, Sci. Rep. 7 (2017) 43340.
[21] COMSOL. COMSOL 5.3 Acoustics Module User's Guide. COMSOL Inc., 2017.
[22] I.B. Crandall, Theory of Vibrating Systems and Sound. Van Nostrand, 1926.
[23] C. Zwikker, C.W. Kosten, Sound Absorbing Materials, Elsevier, 1949.
[24] D.Y. Maa, Theory and design of microperforated panel sound-absorbing constructions, Sci. Sin. 18 (1) (1975) 55–71.
[25] ISO 10534-2: Determination of sound absorption coefficient and impedance in impedance tubes. Part 2: Transfer-function method. 1998.